Reciprocated Electrochemical and DFT Investigations of Iron Selenide: Mechanically Bendable Solid-State Symmetric Supercapacitor

Bidhan Pandit[1,2], Sachin R. Rondiya[3], Shyamal Shegokar[1], Lakshmana K. Bommineedi[1], Russel W. Cross[3], Nelson Y. Dzade[3], Babasaheb R. Sankapal[1]*

[1]Nano Materials and Device Laboratory, Department of Physics, Visvesvaraya National Institute of Technology, South Ambazari Road, Nagpur 440010, Maharashtra, India.

[2]Department of Materials Science and Engineering and Chemical Engineering, Universidad Carlos III de Madrid, Avenida de la Universidad 30, 28911 Leganés, Madrid, Spain.

[3]School of Chemistry, Cardiff University, Main Building, Park Place, Cardiff, CF10 3AT, Wales, United Kingdom.

Abstract

Enhanced energy storing capability with the aid of unique nanostructured morphology is beneficial to enrich the effective path for the development of energy storing capability of supercapacitors. Scheming earth abundant and low-cost transitional metal selenides (TMSs) with enhanced charge transfer capability with pronounced stability is still a challenge. Herein, state of art is presented for iron selenide with nanoflakes surface architecture synthesized with aid of simple, industry-scalable, and ionic layer controlled chemical approach namely; successive ionic layer adsorption and reaction (SILAR) method. Iron selenide electrode yields capacitance of 671.7 F/g at 2 mV/s scan rate and 434.6 F/g at 2 mA/cm^2 current density through cyclic voltammetry (CV) and galvanostatic charge-discharge (GCD) studies, respectively with 91.9% cyclic retention at 4000 cycles. Developed bendable solid-state supercapacitor reveals remarkable power density of 5.1 kW/kg with outstanding deformation tolerance including practical demo to run small fan, demonstrating capability for advanced energy storage applications. Complementary first-principles Density Functional Theory (DFT) approach used to achieve reciprocity with experimental supercapacitive performance through the understandings of the electronic structure.

Keywords: Iron selenide, Flexible supercapacitor, Symmetric cell, Solid-state device, Density functional theory

1. Introduction

Electrochemical supercapacitors entailing superior energy and power densities are crucial for sustainable and large-scale energy storage which is vital in the development of portable electronics, medical devices, and zero-emission transportation.[1, 2] Nanostructured electrode materials have shown excellent electrochemical activities with rapid redox reactions or advanced ion adsorption on surface due to enhanced active electrochemical sites for charge transfer with stable electronic and ionic transport at small-scale diffusion range in producing high-performance supercapacitors.[3]

Numerous attempts have been reported to synthesize mesoporous materials, nanostructured composites, self-assembled micro/nano structures including nanofilms, nanoparticles, nanorods, and hierarchical 3-D conducting web networks.[4-9] Despite the excellent electrochemical activities, nanostructured materials are limited by low electrical conductivity, low rate performance, and poor cyclic stability, which remain a major challenge to the practical applications.[10, 11] So, improved nanostructured materials with steady behavior, better capacitance, and enhanced kinetics are the prime requisites for high-performance supercapacitors.

Recently, transition metal selenides (TMSs) are encouraging as energy storage materials due to intrinsic superior electronic properties, variable oxidation states, excellent electrical conductivities, large specific surface areas, enriched redox active sites, and quick ion transportation.[12, 13] Although metal selenides have analogous characteristics as metal sulfides, the metal selenides possess superior electrical conductivity and density, suggesting higher rate capability and volumetric energy density than the metal sulfides.[14-18] Other merits of TMSs are their earth abundance, low cost, and suitability for assembly, which makes them attractive electrode materials for sustainable energy storage applications. Transition metal diselenides (TMDSs) exhibit typical sandwich type structure consisting of metal atom covalently bonded with two discrete selenide layers. Importantly, the only interactive force (van der Waals force)

among two discrete sheet layers is sufficiently weak to permit electrolyte ions to intercalate simply in inter-chain portions reversibly, thus making intercalated complexes or species to store charge in layered sites. Recently, noteworthy progress have been appreciated in M_xSe_y and corresponding composites towards energy conversion and storage applications.[14] Some binary metal selenides such as $GeSe_2$,[19] CoSe,[20] $MoSe_2$,[21] and $SnSe_2$[22] have reported as electrode for supercapacitor applications. Recently, porous carbon (nitrogen-doped) have been used as negative electrode with NiSe@$MoSe_2$ as positive electrode to fabricate unique asymmetric supercapacitor exhibiting energy density of 32.6 Wh/kg by maintaining power density of 415 W/kg by Hiu et al.[23] In another aspect, $NiCo_2Se_4$ demonstrates high conductivity as compared to $NiCo_2S_4$[24] and $NiCo_2O_4$[25].

However, there exists a limited report of iron selenide as active electrode material for solid-state supercapacitor applications. Iron diselenide exists in two stoichiometric phases: $FeSe_2$ and α-FeSe.[26] Each of the phase have Fe-2p core level electron configuration, and their pure phase-specified synthesis is still a challenge.[27] The stable and homogeneous $FeSe_2$ and α-FeSe phases have diversity of structure and morphology.[28, 29] The α-FeSe has mainly tetragonal structure but also available in hexagonal structure whereas the $FeSe_2$ has orthorhombic structure with high absorption coefficient.[30] Ji et al. prepared $FeSe_2$ supercapacitive material (anode) with snowflake-like morphological hierarchy by anion exchange method that exhibits moderate capacitance of 304 F/g at 0.5 A/g with improved rate capability.[31] Ion-exchange route was involved by Wang et al. to prepare carbon fiber (CF) decorated with $FeSe_2$ nanonuts to achieve 264.6 F/g capacitance at constant current density of 0.45 A/g.[32] Iron diselenide has also been explored for solar cells,[33, 34] lithium and sodium ion batteries,[35, 36] and electrocatalysts for oxygen evolution reaction (OER).[37, 38] In previous studies, different synthesis methods such as chemical vapour deposition, electrodeposition, solvothermal, and hydrothermal have been adopted to prepare iron selenide.[39]

In this communication, the first report on synthesis of nanoflakes surface architecture of iron selenide with aid of simple, industry scalable, and inexpensive successive ionic layer adsorption and reaction (SILAR) method has been focused. Formed nanoflakes surface architecture has been used as an advanced electrode material for fabricating bendable complete solid-state symmetric supercapacitor device using lithium perchlorate ($LiClO_4$) incorporated polyvinyl alcohol (PVA) as polymer gel electrolyte. Bare iron selenide electrode yields specific capacitance of 671.7 F/g (@2 mV/s) with excellent cycling stability in a liquid-electrolyte based three-electrode configuration. Route to fabricate electrodes efficiently resolves the mechanical difficulties to regulate mass loading of electroactive material on stainless steel substrate (SS) along with large scale integration for mass production. Resultant nanoflakes structured iron selenide demonstrates an excellent electrochemical performance when applied in flexible solid-state symmetric supercapacitor configuration.

2. Results and discussion

2.1 Structural Studies: Structural behavior of synthesized iron selenide was identified by X-ray diffraction (XRD) and is depicted in **Figure 1a**. It exhibits two weak peaks at 2θ values of 36.3 and 44.5° corresponding to orthorhombic structured iron selenide with (120), and (121) planes, respectively (JCPDS card no. 21-0432). Obtained weak diffraction pattern is due to inclusion of small crystallites with the preferred orientation (very few crystallites oriented to give diffraction), where nanoflakes morphology is well in support. Coherence length of electrons is much smaller, especially in high resolution transmission electron microscopy (HR-TEM), and hence, the diffraction pattern is easily visible. Hence, the phase confirmation was additionally concluded by using HR-TEM and X-ray photoelectron spectroscopy (XPS) analyses.[40] Crystal structure shown in the inset of **Figure 1a** provides well-defined ion channels which provide nano-network for the fast diffusion of electrolyte ions, beneficial for supercapacitive activities. The element valence states were precisely studied by complete XPS analysis, and associated outcomes are pictured in **Figure 1b, c**. In the Fe 2p core level spectrum

(**Figure 1b**), two significant peaks observed at 710.9 and 723.8 eV are assigned to Fe $2p_{3/2}$ and Fe $2p_{1/2}$, respectively.[40, 41] Characteristic Se 3d peak observed at 55.7 eV is in well agreement with iron selenide reported previously (**Figure 1c**).[42, 43] Appearance of tiny peak at 59.4 eV implicates the inclusion of selenium species might be arises because of the surface-oxidation.[38]

Thermogravimetric analysis (TGA) was studied in air environment at specific heating rate of 10 °C/min from room temperature to 572 °C and results are shown in **Figure 1d**. Slight weight loss has been observed from 200 to 300 °C due to the initial oxidation of iron selenide. Notable weight loss observed from 300 to 500 °C corresponds to the thermal decomposition followed by the oxidation process with the formation of Fe_2O_3, and volatile SeO_2 gas, concluding a total 48 % weight loss.[44] Kong et al. clearly described similar trend for $FeSe_2$ anchored reduced graphene oxide (rGO) composite.[45]

$$4FeSe_2(s) + 11O_2(g) \rightarrow 2Fe_2O_3(s) + 8SeO_2(g) \qquad (1)$$

2.2 Morphological analysis: Electrochemical interaction depends on the surface morphology; hence the surface properties of as-synthesized iron selenide were scanned through field emission scanning electron microscopy (FE-SEM). It is evident from FE-SEM images (**Figure 2a, b**) that the substrate surface was uniformly covered by unique nanoflakes morphology with high surface area beneficial for supercapacitor application.[46, 47] To get clear insights of morphology and local crystallographic properties, HR-TEM analysis was performed (**Figure 2c-e**). The HR-TEM images reveal the formation of extremely uniform and porous nanoflakes web, which is well supported by the FE-SEM morphological information. Such unique nanoflakes surface architecture provides enough voids to electrolyte and effective electron pathways for longitudinal current, which is necessary for efficient supercapacitor applications.[48] As per selected-area electron diffraction (SAED) pattern visualized in **Figure 2e**-inset, the (120) and (121) planes are confirmed by well-defined diffraction patterns; exhibiting well agreement with specified peaks by XRD studies supporting the formation of nanocrystalline phase of iron selenide.

2.3 Supercapacitive performance of iron selenide electrode: The chemical activity of an electrolyte at electrode depends on the ionic mobility, conductivity, hydrated ionic radius, and diffusion rate.[49] All the electrochemical investigations of iron selenide electrode were performed at 0.5 M NaOH electrolyte (**Figure S1**). **Figure 3a** shows the cyclic voltammetry (CV) plots in 100 to 2 mV/s scanning range with a potential frame between -1.3 to -0.4 V. The electrode exhibits intense reduction and oxidation peaks due to fast and reversible redox behaviors, indicating the pseudocapacitive nature of charge storage mechanism.[50, 51] The rectangular CV shape indicates the perfect electric double-layer behavior[52] but obtained CV shape of iron selenide electrode exhibited non-identical rectangular curve with the following redox reaction: [53, 54]

$$FeSe_2 + OH^- \rightarrow FeSe_2OH + e^- \qquad (2)$$

The CV shows stable and analogous shape at higher scan rate (100 mV/s) showing high-power electrochemical reversibility. The iron selenide electrode demonstrates exceptional specific capacitance of 671.7 F/g at fixed scan rate of 2 mV/s (**Figure 3b**). The associated capacity of the electrode with respect to scan rate is also calculated and presented **Figure S2**. At relatively lower scans, the involved electrolyte ions get satisfactory time for diffusion into the active electrode material.[55, 56] Slight shifts in cathodic and anodic peaks respective to their negative and positive potentials with rise in the scan rates exhibiting the polarization along with fast ion transport for the electro active material.

The CV plots of the electrode are additionally investigated in detail to further investigate the dual charge storage mechanism.[57-59] The charge stored associated with electrode is provided by capacitive and diffusion-controlled faradaic contributions. The total charge storage contribution at a fixed potential (V) can be quantified by the combination of diffusion ($k_2v^{1/2}$) and capacitive (k_1v) effects as per the following equations:[60]

$$i = k_1 v + k_2 v^{\frac{1}{2}} \qquad (3)$$

$$\frac{i}{v^{\frac{1}{2}}} = k_1 v^{\frac{1}{2}} + k_2 \qquad (4)$$

where i indicates the current response, v specifies scan rate and k_1, k_2 are the associated constants which can be estimated by plotting $i/v^{1/2}$ versus v. In present case, standard Python numerical programming was employed to get precise calculations by considering all the data points related to CV plots. As presented in **Figure 3c**, it is observed that the diffusion contributions masters over the capacitance-controlled process at relatively low scan rates, specifically, around 92.1 % at 2 mV/s, though the capacitive contributions gradually increase with the increase in scan rates.[61] It is also observed that the diffusion-controlled activities are higher than that of capacitive activities at each specific scan rates, signifying that the diffusion of the electrolyte ions is rather easier than adsorption/desorption process, which is in well agreement in accord with CV outcomes. The shaded area (green) in **Figure 3d** reveals the capacitive contribution of the electrode for 20 mV/s scan rate.

All the Galvanostatic charge-discharge (GCD) plots of iron selenide electrode depicted in **Figure 4a** show three clear parts of voltage variation with time: (i) quick voltage drop because of intrinsic resistance of material, (ii) linear part due to capacitive double layer involvement, and (iii) non-linear section for reversible redox reactions.[62] The symmetrical and sharp discharge plateaus with minor iR drop reflect excellent pseudocapacitive activities; in well agreement with CV outcomes.[63] The electrode reveals excellent specific capacitance of 434.6 F/g at current density of 2 mA/cm^2 (**Figure 4b**). At relatively low current densities, the charge-transfer activities are more deep and associated electrolyte ions can arrive to more active interfaces to assist, so the potential plateau is evidently relatable with longer time in case of comparatively high current densities.[64, 65]

Constant voltage (float) containing ten galvanostatic cycles (5 mA/cm^2, -1.3 to -0.4 V window) and a potentiostatic step at -0.4 V for 1 h (defined as floating step) as shown in **Figure 4c**. The float and cycling steps were repeated continuously along with the detection of

normalized capacitance retention. **Figure 4d** shows the change in capacitance with the total floating time of 10 h. It is noticeable that electrode voltage is steady in the voltage frame with a capacitance retention of 53%. The continuous capacitance decay of electrode maybe associated to higher potential attained by the electrode.[66] Moreover, it is observed that the capacitance drop after first float step was 9% because of decreased ion accessibility (electrolyte starvation effect) or less available electroactive surface area for electrolyte ions.[67] Actually, the gradual fading is related to the functional cut-off potential, the greater the cut-off, the stronger the driving force for unnecessary electrochemical side-reactions, the shorter the cycle lifetime. Moreover, the current may damage the electrode due to the increase in temperature, and many other faradaic side-reactions may be associated with the in inefficient kinetics. The reduction in capacitance can principally be linked to the rise in impedance of the electrode. Perhaps, a change in the structure of material originally arises with the association with equilibration potential. He et al. described the fading phenomena associated with voltage floating test extensively in his article.[68] There are similar kind deteriorates in cell performance shown in previous articles.[69, 70]

The stability of iron selenide electrode was examined by repeated cyclic curves for 4000 cycles recorded through constant 100 mV/s scan rate. The electrode shows a superior capacitive retention by maintaining 91.9% of the prime value even at 4000 CV cycles (**Figure 5a**). Essentially, the good contact associating with electrode material and the current collector interface pointedly diminishes the interactional charge transfer resistance, advancing the utilization rate of material, and subsequently results in excellent supercapacitive activities. The Nyquist plot (Z′ vs. Z″ plot) shown in **Figure 4b** was recorded in the 0.1 to 100 Hz frequency range. The charge transfer resistance (R_{CT}) specified by partial semi-circular curve is mostly reliant on structure and morphology of electro active material.[71, 72] Moreover, the resistance analyzed by intersection point in X-axis signifies the important equivalent series resistance (R_S), and it is evidently related mainly with resistive factors arising at the electrode-electrolyte

interface.[73, 74] The low values of R_S (1.90 Ω/cm^2) and R_{CT} (1.32 Ω/cm^2) are in favor of excellent electrochemical kinetics for the iron selenide electrode. The observed straight line behavior at relatively low-frequency region reveals a first-rate capacitive activities agreeing to the stored charge with low ion diffusion resistance exactly consistent with an ideal capacitor.[75] The simulation outcome in relevance with the equivalent circuit fits properly with the examined result (inset, **Figure 5b**). The semi-infinite nature of diffusion related to electrolyte ions signifies the constant phase element (CPE), whereas the change from high to reasonably lower frequency region is related with Warburg factor (W).[76, 77] The associated relaxation time constant ($\tau_0 = \frac{1}{f_0}$, where f_0 is characteristic frequency) also recognized as supercapacitor figure of merit delivers the information to realize improved electrochemical kinetics.[78] A minor τ_0 value signifies faster power response of electrode in terms of electrochemical activities, can be derived by the maximum Gaussian peak from imaginary component of capacitance (C'') with concerning frequency (f) plot.[79, 80] The estimated τ_0 value of 2.97 ms (**Figure 5c**) clearly indicates fast ion mobility of free carriers. Additionally, Bode phase diagram in **Figure 5d** shows a linear trajectory by ensuring a sharp change in phase angle from high to relatively lower frequency region, corresponds to excellent pseudocapacitive behavior. Obtained phase angle of -77.7° in the low-frequency region falls between −45° (pseudocapacitors) and −90° (ideal capacitor), which evidences the presence of intercalation/de-intercalation capacitance in electrode.[81, 82] The critical factor of merit for supercapacitor can be further analyzed by relaxation time constant τ_0, which can be evaluated by $\tau_0 = \frac{1}{f_0}$ when the associated phase angle is -45°.[83] The τ_0 is calculated to be about 1.74 ms, signifying that the energy storage properties is pure capacitive below this specific frequency.[84]

2.4 Performance of flexible solid-state symmetric supercapacitor device: Bendable electrochemical supercapacitor with excellent electrical stability and high mechanical strength is still a great challenge.[85, 86] Benefiting from its exceptional electrochemical properties, the

newly developed iron selenide electrode can be used to fabricate symmetric flexible solid-state supercapacitor assembled using PVA-$LiClO_4$ gel electrolyte. The solid-state devices constructed with solid electrolyte alternative to liquid electrolyte cell has maximum safety advantages in terms of leakage and sealing as it is free from solvent evaporation.[87] Furthermore, solid-state system can exhibit a long cycle-life along with mechanical flexibility (bendable) approach that can be possible to integrate with portable electronics. The schematic of formed symmetric solid-state device arrangement with PVA/$LiClO_4$ gel electrolyte is depicted as inset of **Figure 6a**. A preliminary study of the PVA-$LiClO_4$ electrolyte shows excellent viscosity of 45 cP, ionic conductivity of 11.4 ± 0.20 mS/cm, and wide potential window 4.1 V.[88] Additionally, the pseudocapacitive nature of iron selenide electrode in specific PVA-$LiClO_4$ gel electrolyte relies on the intercalation/extraction action of cations. A sequence of CV plots of the fabricated supercapacitor at various voltage frames staring from 0 to 1.8 V at fixed 100 mV/s scan rate were recorded to improve the suitable voltage window as revealed by **Figure 6b**. The best capacitances of 65.3 F/g at a scan rate of 2 mV/s and 24.4 F/g at a scan rate of 100 mV/s have been achieved. The observed degradation in the capacitance is due to the less involvement of electroactive material throughout electrochemical reactions as diffusion time of participated electrolyte ions into material is limited at higher scan rates.[89] Similarly, **Figure 6c** displays the charge-discharge plots of constructed cell in the voltage frame starting from 0 to 1.8 V at different current densities in the range of 1-2.5 mA/cm^2. Prominently, the device exhibits superior capacitance of 29.8 F/g at projected current density of 1 mA/cm^2 (**Figure 6d**).

The calculated values of capacitance allow to estimate energy and power densities, as they are the critical aspects of supercapacitor. The assembled supercapacitor shows excellent energy density of 13.4 Wh/kg (considering both electrodes mass) at a power density of 2.0 kW/kg, and it remains 8.8 Wh/kg at 5.1 kW/kg (**Figure 7a**). Obtained values of the power and energy densities of solid-state devices are also compared with literature values.[31, 90-96] **Table S1** compares the performance of our lab-made cell with previously reported solid-state

symmetric supercapacitors based on gel electrolytes. No reasonable change in resistance is observed during investigation of electrochemical impedance spectroscopy (EIS) for fabricated device. Small R_S and R_{CT} values are advantageous for first-rate electrochemical performances because of rapid charge transfer with superior conductivity, which can quicken the associated reversible redox activities. Especially, the R_S value of symmetric full cell in high frequency section is ~5.6 Ω that is slightly higher as compared to the three-electrode system (**Figure 7b)**. The outcome specifies that the resistive factors between the electrolyte and electrode in a full cell are enlarged as a consequence of solid-state cell configuration. The R_{CT} value has also increased up to ~2.1 Ω for the device configuration. To examine the mechanical distortion dependent electrochemical performance, the constructed device was taken through various mechanical bending conditions (0, 90, and 175°) and the associated CV plots validate no apparent change in performance of the device under various bending states (**Figure 7c**). It is concluded that, the cell can be easily bent up to 175° deprived of disrupting its physical aspect. The mechanical strength of the cell is accredited to straight connection of electroactive material with stainless steel (SS) substrate and PVA-$LiClO_4$ electrolyte as it constructs H_2 bonds with the water molecules to diminish the capacitance loss by keeping water evaporation away.[97] Besides, gel electrolyte prevents supercapacitor cell from environmental impact and decreases chemical dissolution of active electrode material, upsurges mechanical stability.[89] These results indicate that the device possesses exceptional flexibility and can encounter the necessities of future flexible electronics. A self-made mechanical energy drive system was assembled with the connection of commercially available DC motor fan (1.5 V) directly connected to the manufactured cell. As shown in **Figure 7d**, the single cell can drive the mini fan for 15 seconds after being charged (**supporting video**). So, the proof-of-concept demonstration of fabricated mechanical power system evidently illustrates the feasible and potential prospects in energy storage application.

2.5 First-principles calculations: Iron selenide was modelled in orthorhombic structure (**Figure 8a**) with the space group *Pnnm* (No. 58). The optimized lattice parameters are projected at a = 4.751 Å, b = 5.743 Å, and c = 3.580 Å, all of which are in well agreement with the experimental lattice parameters: a = 4.800 Å, b = 5.782 Å, and c = 3.583 Å.[98] The calculated band structure (**Figure 8b**) exhibits indirect band gap of iron selenide with predicted band gap of 1.05 eV. This compares closely with known experimental data (0.95–1.03)[98] and previous DFT calculations.[99] The conduction and valence band edges are mainly composed of Fe-3*d* states with a minute involvement of S-3*p* states as analyzed by projected partial density of states as depicted in **Figure 8c**. Considering that we are dealing with an electrode material where surfaces play important role, the structures and stabilities of the (001), (100) and (120) surfaces of iron selenide were systematically characterized as shown in **Figure 9(a-c)**. The surface energy of the (001), (100) and (120) surfaces is estimated at 1.18, 1.37, 1.24 Jm^{-2}, indicating that the (001) is the most stable surface and the (100) is the least stable surface among the three surfaces investigated. It is obvious from electronic density of states (**Figure 9d**) that whereas the (100) surface remain semiconducting (E_g =0.73 eV), the (001) and (120) surface display metallic characteristics as reflected in the continuous available states at the Fermi level (although very small). From the DFT-computed DOS, the quantum capacitance (C_Q) has been analyzed following the expression:

$$C_Q = e^2 \int_{-\infty}^{+\infty} D(E) F_T(E - e\emptyset_G) dE \quad (3)$$

where *D(E)* is DOS of the concerned surface; $\emptyset_G$ is the electrode potential; and $F_T(E)$ specifies the thermal broadening function, which is expressed as

$$F_T(E) = (4K_BT)^{-1} sech^2\left(\frac{E}{2K_BT}\right) \quad (4)$$

The quantum capacitance (C_Q) plot with respect to electrode potential function for three different iron selenide surfaces are depicted in **Figure 9e**. It can be seen that the quantum capacitance is surface dependent, where the (001) surface displays higher C_Q values at almost

all applied potentials compared to the (100) and (120) surfaces. The trend of the predicted quantum capacitance for the different surfaces is consistent with their DOS plot.

3. Conclusions

A suite of complementary experimental and computational techniques has been systematically reciprocated to examine the structural, electronic and electrochemical properties of iron selenide thin films. The excellent pseudocapacitive activity of the iron selenide electrode was accredited to its unique porous nanoflakes surface architecture. The superior specific capacitance of 671.7 F/g (2 mV/s) of the electrode highlights that the involvement of conductive iron selenide provides not only a better capacitance but also an exposed web for effective electrolyte diffusion to exhibit exceptional stability in spite of redox-active interactions. The assembled flexible supercapacitor shows a superior capacitance of 65.3 F/g, a superior energy density of 13.4 Wh/kg and highest power density of 5.1 kW/kg with a remarkable potential limit of 1.8 V. The quantum capacitance predicted from electronic density functional theory calculation shows that the capacitance performance is sensitive to the exposed surface of the iron selenide electrode. Apart from the superior supercapacitive performance, the magnificent flexibility (175°) originating from the excellent mechanical robustness of electrode-electrolyte system marks the iron selenide based supercapacitor as an attractive energy storage candidate in flexible electronics.

4. Experimental parameters

4.1 Electrode development: Simple SILAR method was involved to synthesize iron selenide thin film on SS substrate by using 50 mM iron sulphate ($FeSO_4.7H_2O$, cationic solution) complexed with oxalic acid ($C_2H_2O_4$) and sodium selenosulfate (Na_2SeSO_3, anionic precursor). The Na_2SeSO_3 was prepared by using simple reflux method for 10 hours at 90 ^oC using crushed selenium ingots and sodium sulphite (ratio 5:15) in double distilled water (DDW). Furthermore, 2 ml of prepared Na_2SeSO_3 was added in 48 ml of DDW under constant stirring, and further used for final anionic precursor. Mirror polished SS substrate was vertically immersed in

cationic precursor and then rinsed in DDW to eradicate loosely adherent species. Next, the pre-adsorbed substrate was inserted in anionic precursor (at 80 ^{o}C), and again rinsed in DDW to remove over growth particles. Finally, the ionic cluster of intermediate iron selenide has nucleated with formation of critical radius and accomplished in thin film form in 40 number of SILAR cycles followed by annealing process (200 ^{o}C for 1h) with the following specified reaction mechanism:

Na_2SeSO_3 (pH>8.5) in association with present hydroxide ions provides Se^{2-} ions.[100]

$$Na_2SeSO_3 + OH^- \rightarrow Na_2SO_4 + HSe^- \quad (5)$$

$$HSe^- + OH^- \rightarrow Se^{2-} + H_2O \quad (6)$$

Importantly, the capability of the precursor solution to produce Se^{2-} ions is mainly rely on the concentration of alkaline medium. Moreover, the Se^{2-} ions assocaite with the Se elemental residue to provide Se_x^{2-} ions at 80 ^{o}C.

$$Se^{2-} + Se = Se_2^{2-} \quad (7)$$

The iron selenide was obtained after the final and most important anneal process followed by the intermediate complex reaction step. The possible reaction mechanism in the anneal step:

$$Fe^{2+} + Se_2^{2-} = FeSe_2 \quad (8)$$

The similar kind of typical solution based reaction mechanism is explained briefly in previous reports.[101-103]

4.2 Characterizations, electrochemical studies and device fabrication: Structural studies were performed by using the X-ray diffractometer (Bruker AXS D8 Advance) using copper (K_α) radiation with wavelength λ = 1.5406 Å. Chemical phase analysis were performed by XPS PHI 5000 VersaProbe II (ULVAC INC). TGA was performed by using SII 6300 EXSTAR. FE-SEM was engaged to study the surface morphology with the help of JEOL-JSM 6360 unit. For clearer insights, HR-TEM was performed by using JEOL 2100 with LaB_6 source. PARSTAT 4000 electrochemical work-station was used for evaluating electrochemical characteristics such as CV, GCD, and EIS. Standard equations were used to estimate the associated electrochemical

parameters (**Supporting discussion**). The exact mass loading on SS substrate was 0.88 mg for 2×2 cm^2 surface. PVA-$LiClO_4$ gel electrolyte was formulated to fabricate solid-state device by addition of $LiClO_4$ (3 g) and PVA (3 g) into deionized DDW (30 ml).[104] A specific heat treatment of 90 °C with vigorous stirring made the solution viscous and clear. Afterwards, the prepared gel was used to paint on iron selenide coated films uniformly. These two similar films were packaged in sandwich structure to construct bendable symmetric solid-state cell and kept in fume hood under constant pressure of one ton until gel electrolyte got solidified.

4.3 Computational Details: The optimized bulk and surface structures were analyzed with the help of plane-wave density functional theory (PW-DFT) simulations as applied in the VASP package.[105-107] The projected augmented wave (PAW) method was considered to determine the association among the ionic core and valence electrons[108] and Perdew–Burke–Ernzerhof (PBE) generalized gradient approximation (GGA) functional[109] using Hubbard U correction (PBE+U)[110, 111] was involved to analyze the electronic exchange–correlation potential. An effective U= 2 eV has been found to illustrate the precise explanation of electronic properties and structural parameters of iron selenide, which is consistent with previous calculation for marcasite FeS_2.[112-114] For entire analysis, the dispersion forces were considered through Grimme DFT-D3 functional.[115] To converge the total energy of iron selenide within 10^6 eV, a plane-wave basis set with an adequate kinetic energy cutoff of 600 eV was examined and associated residual Hellman–Feynman forces were converged in the ionic relaxations within 10^3 eV $Å^{-1}$. Moreover, the Brillouin zone was tested by using a 7 x 5 x 3 mesh of Monkhorst–Pack k-points.[116] The k-meshes were selected for surface calculations in such a manner that a analogous spacing of associated points in the related reciprocal space was sustained.

Acknowledgements

This study is funded in part by a grant from DST/TMD/MES/2k16/09 project, Government of India. B.P. acknowledges the CONEX-Plus programme funded by Universidad Carlos III de Madrid (UC3M) and the European Commission through the Marie-Sklodowska

Curie COFUND Action (Grant Agreement No 801538). SRR and NYD appreciate the UK Engineering and Physical Sciences Research Council (EPSRC) for funding (Grant No. EP/S001395/1). Dr Andrew J. Logsdail from Cardiff University is thanked for his assistance with the quantum capacitance calculations. Presented research is supported by the computational facilities of the Advanced Research Computing at Cardiff (ARCCA) Division, Cardiff University, and HPC Wales. This work also used the facilities of the ARCHER (http://www.archer.ac.uk), the national supercomputing service of UK through the membership of HEC Materials Chemistry Consortium funded by EPSRC (EP/L000202).

Additional information

Competing financial interests: The authors declare no competing financial interests.

References

1. Z. Wu, L. Li, J.-m. Yan and X.-b. Zhang, *Adv. Sci.*, 2017, **4**, 1600382.
2. F. Soavi, L. G. Bettini, P. Piseri, P. Milani, C. Santoro, P. Atanassov and C. Arbizzani, *J. Power Sources*, 2016, **326**, 717-725.
3. Z. Yu, L. Tetard, L. Zhai and J. Thomas, *Energy Environ. Sci.*, 2015, **8**, 702-730.
4. R. Liu, J. Duay and S. B. Lee, *Chem. Commun.*, 2011, **47**, 1384-1404.
5. J. H. Fendler, *Chem. Mater.*, 1996, **8**, 1616-1624.
6. Q. Wang, H. Yang, T. Meng, J. Yang, B. Huang, F. L. Gu, S. Zhang, C. Meng and Y. Tong, *Energy Storage Mater.*, 2021, **36**, 365-375.
7. Q. Wang, Y. Li, T. Meng, B. Huang, L. Hu, H. Su, C. Meng and Y. Tong, *ACS Appl. Energy Mater.*, 2021, **4**, 1548-1559.
8. Q. Wang, Y. Zhang, H. Jiang, X. Li, Y. Cheng and C. Meng, *Chem. Eng. J.*, 2019, **362**, 818-829.
9. T. Meng, B. Li, Q. Wang, J. Hao, B. Huang, F. L. Gu, H. Xu, P. Liu and Y. Tong, *ACS Nano*, 2020, **14**, 7066-7076.
10. X.-Y. Yu, L. Yu, L. Shen, X. Song, H. Chen and X. W. Lou, *Adv. Funct. Mater.*, 2014, **24**, 7440-7446.
11. J. Kang, A. Hirata, H.-J. Qiu, L. Chen, X. Ge, T. Fujita and M. Chen, *Adv. Mater.*, 2014, **26**, 269-272.
12. H. Wang, X. Liang, J. Wang, S. Jiao and D. Xue, *Nanoscale*, 2020, **12**, 14-42.
13. H. Chen, S. Chen, M. Fan, C. Li, D. Chen, G. Tian and K. Shu, *J. Mater. Chem. A*, 2015, **3**, 23653-23659.
14. H. Zhou, X. Li, Y. Li, M. Zheng and H. Pang, *Nano-Micro Letters*, 2019, **11**, 40.
15. Z. Li, L. Y. Zhang, L. Zhang, J. Huang and H. Liu, *Nanoscale Res. Lett.*, 2019, **14**, 358.
16. T. Lu, S. Dong, C. Zhang, L. Zhang and G. Cui, *Coord. Chem. Rev.*, 2017, **332**, 75-99.
17. A. Eftekhari, *Sustain. Energy Fuels*, 2017, **1**, 14-29.

18. C. V. V. Muralee Gopi, A. E. Reddy and H.-J. Kim, *J. Mater. Chem. A*, 2018, **6**, 7439-7448.

19. X. Wang, B. Liu, Q. Wang, W. Song, X. Hou, D. Chen, Y.-b. Cheng and G. Shen, *Adv. Mater.*, 2013, **25**, 1479-1486.

20. H. Peng, G. Ma, K. Sun, Z. Zhang, J. Li, X. Zhou and Z. Lei, *J. Power Sources*, 2015, **297**, 351-358.

21. S. K. Balasingam, J. S. Lee and Y. Jun, *Dalton Trans.*, 2015, **44**, 15491-15498.

22. C. Zhang, H. Yin, M. Han, Z. Dai, H. Pang, Y. Zheng, Y.-Q. Lan, J. Bao and J. Zhu, *ACS Nano*, 2014, **8**, 3761-3770.

23. H. Peng, J. Zhou, K. Sun, G. Ma, Z. Zhang, E. Feng and Z. Lei, *ACS Sustain. Chem. Eng.*, 2017, **5**, 5951-5963.

24. Z. Li, N. Chen, H. Mi, J. Ma, Y. Xie and J. Qiu, *Chem. Eur. J.*, 2017, **23**, 13474-13481.

25. Y. Zhang, F. He and X. Li, *J. Taiwan Inst. Chem. Engrs.*, 2016, **65**, 304-311.

26. J. Xu, K. Jang, J. Lee, H. J. Kim, J. Jeong, J.-G. Park and S. U. Son, *Crys. Growth Des.*, 2011, **11**, 2707-2710.

27. B. Ouertani, J. Ouerfelli, M. Saadoun, M. Zribi, M. B. Rabha, B. Bessaïs and H. Ezzaouia, *Thin Solid Films*, 2006, **511-512**, 457-462.

28. O. Kubaschewski, *IRON—Binary Phase Diagrams*, Springer Berlin Heidelberg, 2013.

29. M. Hansen, *Co., New York*, 1985, 502.

30. B. Ouertani, J. Ouerfelli, M. Saadoun, B. Bessaïs, H. Ezzaouia and J. C. Bernède, *Sol. Energy Mater. Sol. Cells*, 2005, **87**, 501-511.

31. C. Ji, F. Liu, L. Xu and S. Yang, *J. Mater. Chem. A*, 2017, **5**, 5568-5576.

32. Q. Wang, Y. Ma, X. Liang, D. Zhang and M. Miao, *Chem. Eng. J.*, 2019, **371**, 145-153.

33. S. Huang, Q. He, W. Chen, Q. Qiao, J. Zai and X. Qian, *Chem. Eur. J.*, 2015, **21**, 4085-4091.

34. S. Huang, Q. He, W. Chen, J. Zai, Q. Qiao and X. Qian, *Nano Energy*, 2015, **15**, 205-215.

35. Z. Zhang, X. Shi, X. Yang, Y. Fu, K. Zhang, Y. Lai and J. Li, *ACS Appl. Mater. Interfaces*, 2016, **8**, 13849-13856.

36. J. S. Cho, J.-K. Lee and Y. C. Kang, *Sci. Rep.*, 2016, **6**, 23699.

37. G. Zhu, X. Xie, X. Li, Y. Liu, X. Shen, K. Xu and S. Chen, *ACS Appl. Mater. Interfaces*, 2018, **10**, 19258-19270.

38. Z. Yang, J.-Y. Zhang, Z. Liu, Z. Li, L. Lv, X. Ao, Y. Tian, Y. Zhang, J. Jiang and C. Wang, *ACS Appl. Mater. Interfaces*, 2017, **9**, 40351-40359.

39. Y. Xie, L. Zhu, X. Jiang, J. Lu, X. Zheng, W. He and Y. Li, *Chem. Mater.*, 2001, **13**, 3927-3932.

40. C. Panda, P. W. Menezes, C. Walter, S. Yao, M. E. Miehlich, V. Gutkin, K. Meyer and M. Driess, *Angew. Chem. Int. Ed.*, 2017, **56**, 10506-10510.

41. J. S. Cho, J.-K. Lee and Y. C. Kang, *Sci. Rep.*, 2016, **6**, 23699.

42. G. D. Park, J. S. Cho, J.-K. Lee and Y. C. Kang, *Sci. Rep.*, 2016, **6**, 22432.

43. B. Yu, J. Jin, H. Wu, S. Wang, Q. Xia and H. Liu, *Int. J. Hydrogen Energy*, 2017, **42**, 236-242.

44. C. An, Y. Yuan, B. Zhang, L. Tang, B. Xiao, Z. He, J. Zheng and J. Lu, *Adv. Energy Mater.*, 2019, **9**, 1900356.

45. F. Kong, L. Lv, Y. Gu, S. Tao, X. Jiang, B. Qian and L. Gao, *J. Mater. Sci.*, 2019, **54**, 4225-4235.

46. X. Chen, C. Wang, M. Song, J. Ma, T. Ye and W. Xia, *Carbon*, 2019, **155**, 521-530.

47. X. Yao and Y. Zhao, *Chem*, 2017, **2**, 171-200.

48. M. Sun, Z. Li, Q. Fang, S. Han, C. Cai, H. Li, W. Shen, X. Liu and Y. Fu, *J. Mater. Chem. A*, 2020, **8**, 724-734.

49. J. Zhu, Y. Xu, J. Wang, J. Lin, X. Sun and S. Mao, *Phys. Chem. Chem. Phys.*, 2015, **17**, 28666-28673.

50. Y. Kim, E.-s. Cho, S.-J. Park and S. Kim, *J. Ind. Eng. Chem.*, 2016, **33**, 108-114.

51. S. A. Pande, B. Pandit and B. R. Sankapal, *Mater. Lett.*, 2017, **209**, 97-101.

52. B. Pandit, S. R. Dhakate, B. P. Singh and B. R. Sankapal, *Electrochim. Acta*, 2017, **249**, 395-403.

53. A. Mohammadi Zardkhoshoui, S. S. Hosseiny Davarani, M. Maleka Ashtiani and M. Sarparast, *J. Mater. Chem. A*, 2019, **7**, 10282-10292.

54. Z. Sun, X. Yang, H. Lin, F. Zhang, Q. Wang and F. Qu, *Inorg. Chem. Front.*, 2019, **6**, 659-670.

55. A. Eftekhari, *ACS Sustain. Chem. Eng.*, 2019, **7**, 3692-3701.

56. K. Lee, D. Kim, Y. Yoon, J. Yang, H.-G. Yun, I.-K. You and H. Lee, *RSC Adv.*, 2015, **5**, 60914-60919.

57. Y. Lan, H. Zhao, Y. Zong, X. Li, Y. Sun, J. Feng, Y. Wang, X. Zheng and Y. Du, *Nanoscale*, 2018, **10**, 11775-11781.

58. D. Du, R. Lan, K. Xie, H. Wang and S. Tao, *RSC Adv.*, 2017, **7**, 13304-13311.

59. Y. Liu, L. Zhang, D. Liu, W. Hu, X. Yan, C. Yu, H. Zeng and T. Shen, *Nanoscale*, 2019, **11**, 15497-15507.

60. F. Yu, Z. Liu, R. Zhou, D. Tan, H. Wang and F. Wang, *Mater. Horiz.*, 2018, **5**, 529-535.

61. S. Dong, L. Shen, H. Li, P. Nie, Y. Zhu, Q. Sheng and X. Zhang, *J. Mater. Chem. A*, 2015, **3**, 21277-21283.

62. B. Pandit, V. S. Devika and B. R. Sankapal, *J. Alloys Compd.*, 2017, **726**, 1295-1303.

63. A. Pendashteh, M. S. Rahmanifar, R. B. Kaner and M. F. Mousavi, *Chem. Commun.*, 2014, **50**, 1972-1975.

64. K. Qi, Y. Qiu and X. Guo, *Electrochim. Acta*, 2014, **137**, 685-692.

65. Y. Q. Wu, X. Y. Chen, P. T. Ji and Q. Q. Zhou, *Electrochim. Acta*, 2011, **56**, 7517-7522.

66. Q. Abbas, D. Pajak, E. Frąckowiak and F. Béguin, *Electrochim. Acta*, 2014, **140**, 132-138.

67. A. Bello, F. Barzegar, M. J. Madito, D. Y. Momodu, A. A. Khaleed, T. M. Masikhwa, J. K. Dangbegnon and N. Manyala, *Electrochim. Acta*, 2016, **213**, 107-114.

68. M. He, K. Fic, E. Frąckowiak, P. Novák and E. J. Berg, *ChemElectroChem*, 2019, **6**, 566-573.

69. P. Ratajczak, K. Jurewicz, P. Skowron, Q. Abbas and F. Béguin, *Electrochim. Acta*, 2014, **130**, 344-350.

70. P. Ratajczak, K. Jurewicz and F. Béguin, *J. Appl. Electrochem.*, 2014, **44**, 475-480.

71. Y. Li, Y. Xia, K. Liu, K. Ye, Q. Wang, S. Zhang, Y. Huang and H. Liu, *ACS Appl. Mater. Interfaces*, 2020, **12**, 25494-25502.

72. Y. Li, K. Liu, J. Zhang, J. Yang, Y. Huang and Y. Tong, *Ind. Eng. Chem. Res.*, 2020, **59**, 18865-18872.

73. A. A. Yadav, A. C. Lokhande, J. H. Kim and C. D. Lokhande, *J. Ind. Eng. Chem.*, 2017, **56**, 90-98.

74. S. A. Pande, B. Pandit and B. R. Sankapal, *Mater. Des.*, 2019, **182**, 107972.

75. V. T. Le, H. Kim, A. Ghosh, J. Kim, J. Chang, Q. A. Vu, D. T. Pham, J.-H. Lee, S.-W. Kim and Y. H. Lee, *ACS Nano*, 2013, **7**, 5940-5947.

76. B. Pandit, S. A. Pande and B. R. Sankapal, *Chin. J. Chem* . 2019, **37**, 1279-1286.

77. B. Pandit and B. R. Sankapal, *New J. Chem.*, 2017, **41**, 10808-10814.

78. D. W. Kim, S. M. Jung and H. Y. Jung, *J. Power Sources*, 2020, **448**, 227422.

79. T. Li, M. Beidaghi, X. Xiao, L. Huang, Z. Hu, W. Sun, X. Chen, Y. Gogotsi and J. Zhou, *Nano Energy*, 2016, **26**, 100-107.

80. S. A. Pande, B. Pandit and B. R. Sankapal, *J. Colloid Interface Sci.*, 2018, **514**, 740-749.

81. Y. Zhang, H. Chen, S. Wang, X. Zhao and F. Kong, *Microporous Mesoporous Mater.*, 2020, **297**, 110032.

82. B. Pandit, G. K. Sharma and B. R. Sankapal, *J. Colloid Interface Sci.*, 2017, **505**, 1011-1017.

83. Z. Zhang, M. Lu, J. Wang, L. Kang and Z.-H. Liu, *Colloids Surf. A: Physicochem. Eng. Asp.*, 2020, **586**, 124232.

84. S.-C. Wang, D. Xiong, C. Chen, M. Gu and F.-Y. Yi, *J. Power Sources*, 2020, **450**, 227712.

85. M.-S. Balogun, W. Qiu, F. Lyu, Y. Luo, H. Meng, J. Li, W. Mai, L. Mai and Y. Tong, *Nano Energy*, 2016, **26**, 446-455.

86. Y. Huang, H. Yang, T. Xiong, D. Adekoya, W. Qiu, Z. Wang, S. Zhang and M. S. Balogun, *Energy Storage Mater.*, 2020, **25**, 41-51.

87. A. Hayashi, T. Ohtomo, F. Mizuno, K. Tadanaga and M. Tatsumisago, *Electrochem. Commun.*, 2003, **5**, 701-705.

88. S. Abarna and G. Hirankumar, *Ionics*, 2017, **23**, 1733-1743.

89. Y. V. Kaneti, J. Tang, R. R. Salunkhe, X. Jiang, A. Yu, K. C.-W. Wu and Y. Yamauchi, *Adv. Mater.*, 2017, **29**, 1604898.

90. M. S. Javed, S. S. A. Shah, S. Hussain, S. Tan and W. Mai, *Chem. Eng. J.*, 2020, **382**, 122814.

91. D. B. Malavekar, S. B. Kale, V. C. Lokhande, U. M. Patil, J. H. Kim and C. D. Lokhande, *J. Phys. Chem. C*, 2020, **124**, 28395-28406.

92. Y. Qiu, X. Li, M. Bai, H. Wang, D. Xue, W. Wang and J. Cheng, *Inorg. Chem. Front.*, 2017, **4**, 675-682.

93. T. T. Nguyen, J. Balamurugan, V. Aravindan, N. H. Kim and J. H. Lee, *Chem. Mater.*, 2019, **31**, 4490-4504.

94. A. K. Das, S. Paria, A. Maitra, L. Halder, A. Bera, R. Bera, S. K. Si, A. De, S. Ojha, S. Bera, S. K. Karan and B. B. Khatua, *ACS Appl. Electron. Mater.*, 2019, **1**, 977-990.

95. Q. Zong, Y. Zhu, Q. Wang, H. Yang, Q. Zhang, J. Zhan and W. Du, *Chem. Eng. J.*, 2020, **392**, 123664.

96. D. B. Malavekar, R. N. Bulakhe, S. B. Kale, U. M. Patil, I. In and C. D. Lokhande, *J. Alloys Compd.*, 2021, **869**, 159198.

97. M. S. Javed, Z. Jiang, Q. Yang, X. Wang, X. Han, C. Zhang, X. Gu and C. Hu, *Electrochim. Acta*, 2019, **295**, 558-568.

98. A. Kjekshus, T. Rakke and A. F. Andresen, *Acta Chem. Scand.*, 1974, **28a**, 996-1000.

99. B. Ganga, C. Ganeshraj, A. G. Krishna and P. Santhosh, *arXiv preprint arXiv:1303.1381*, 2013.

100. S. Ananthakumar, J. R. Kumar and S. M. Babu, *J. Inorg. Organomet. Polym. Mater.*, 2017, **27**, 569-575.

101. K. Liu, H. Liu, J. Wang and L. Feng, *Mater. Lett.*, 2009, **63**, 512-514.

102. H. Zhang, B. Yang, X. Wu, Z. Li, L. Lei and X. Zhang, *ACS Appl. Mater. Interfaces*, 2015, **7**, 1772-1779.

103. W. Zhang, Z. Yang, J. Liu, Z. Hui, W. Yu, Y. Qian, G. Zhou and L. Yang, *Mater. Res. Bull.*, 2000, **35**, 2403-2408.

104. B. Pandit, N. Kumar, P. M. Koinkar and B. R. Sankapal, *J. Electroanal. Chem.*, 2019, **839**, 96-107.

105. G. Kresse and J. Hafner, *Phys. Rev. B*, 1993, **47**, 558-561.

106. G. Kresse and D. Joubert, *Phys. Rev. B*, 1999, **59**, 1758-1775.

107. G. Kresse and J. Furthmüller, *Phys. Rev. B*, 1996, **54**, 11169-11186.

108. P. E. Blöchl, *Phys. Rev. B*, 1994, **50**, 17953-17979.

109. J. P. Perdew, K. Burke and M. Ernzerhof, *Phys. Rev. Lett.*, 1997, **78**, 1396-1396.

110. A. Rohrbach, J. Hafner and G. Kresse, *J. Phys.: Condens. Matter*, 2003, **15**, 979-996.

111. V. I. Anisimov, F. Aryasetiawan and A. I. Lichtenstein, *J. Phys.: Condens. Matter*, 1997, **9**, 767-808.

112. N. Y. Dzade and N. H. de Leeuw, *Phys. Chem. Chem. Phys.*, 2017, **19**, 27478-27488.

113. L. Wu, N. Y. Dzade, L. Gao, D. O. Scanlon, Z. Öztürk, N. Hollingsworth, B. M. Weckhuysen, E. J. M. Hensen, N. H. de Leeuw and J. P. Hofmann, *Adv. Mater.*, 2016, **28**, 9602-9607.

114. R. Sun, M. K. Y. Chan and G. Ceder, *Phys. Rev. B*, 2011, **83**, 235311.

115. S. Grimme, J. Antony, S. Ehrlich and H. Krieg, *J. Chem. Phys.*, 2010, **132**, 154104.

116. H. J. Monkhorst and J. D. Pack, *Phys. Rev. B*, 1976, **13**, 5188-5192.

Figures

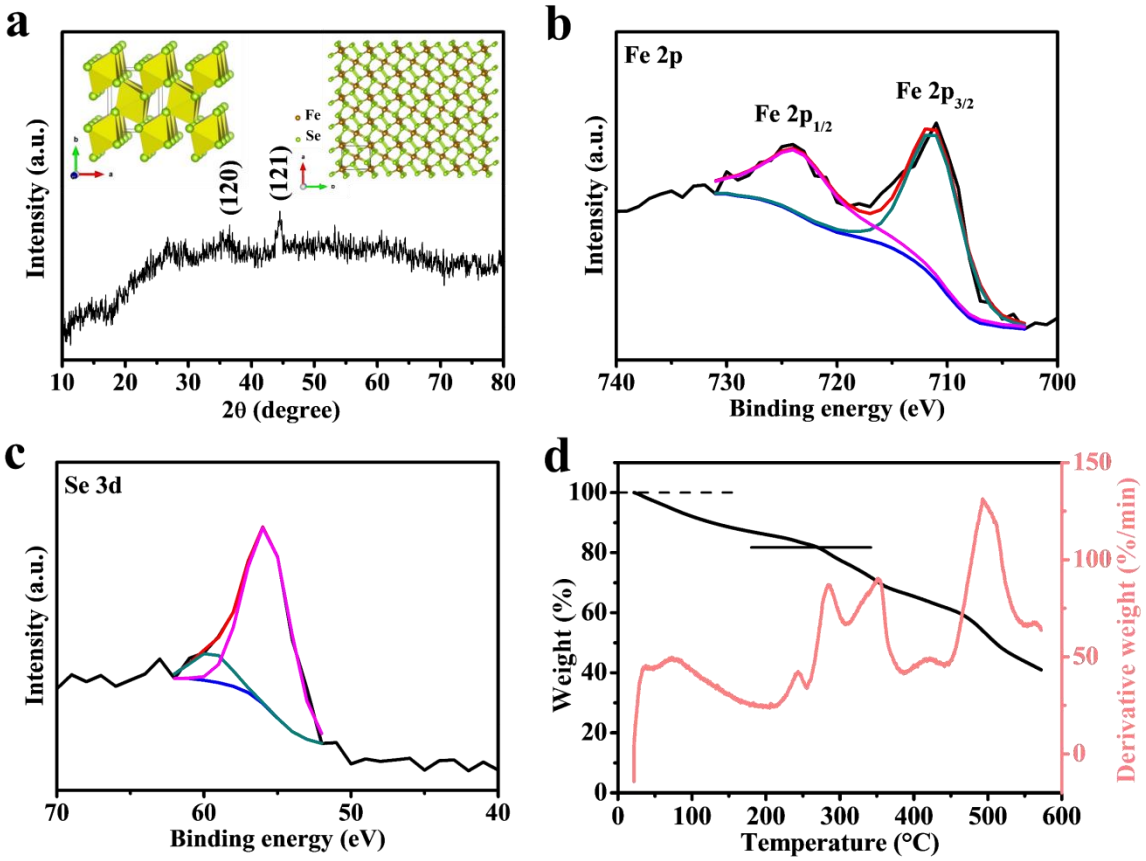

Figure 1 (a) Typical XRD pattern of iron selenide powder sample, inset shows associated crystal structure. (b, c) Core level XPS spectra of Fe 2p and Se 3d of iron selenide thin film. (d) TGA graph of iron selenide.

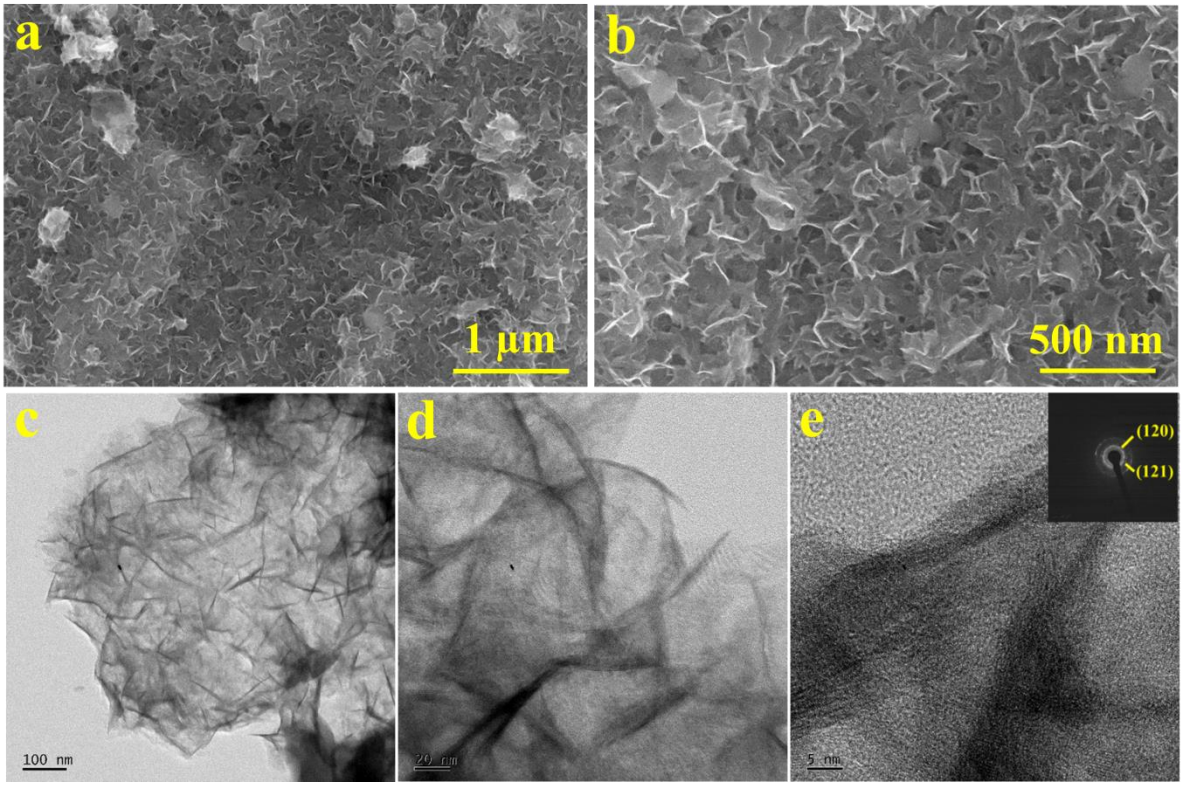

Figure 2 (a, b) FE-SEM images of iron selenide thin film at different magnifications. (c-e) HR-TEM images of iron selenide Sample, inset of Figure 2e shows SAED pattern.

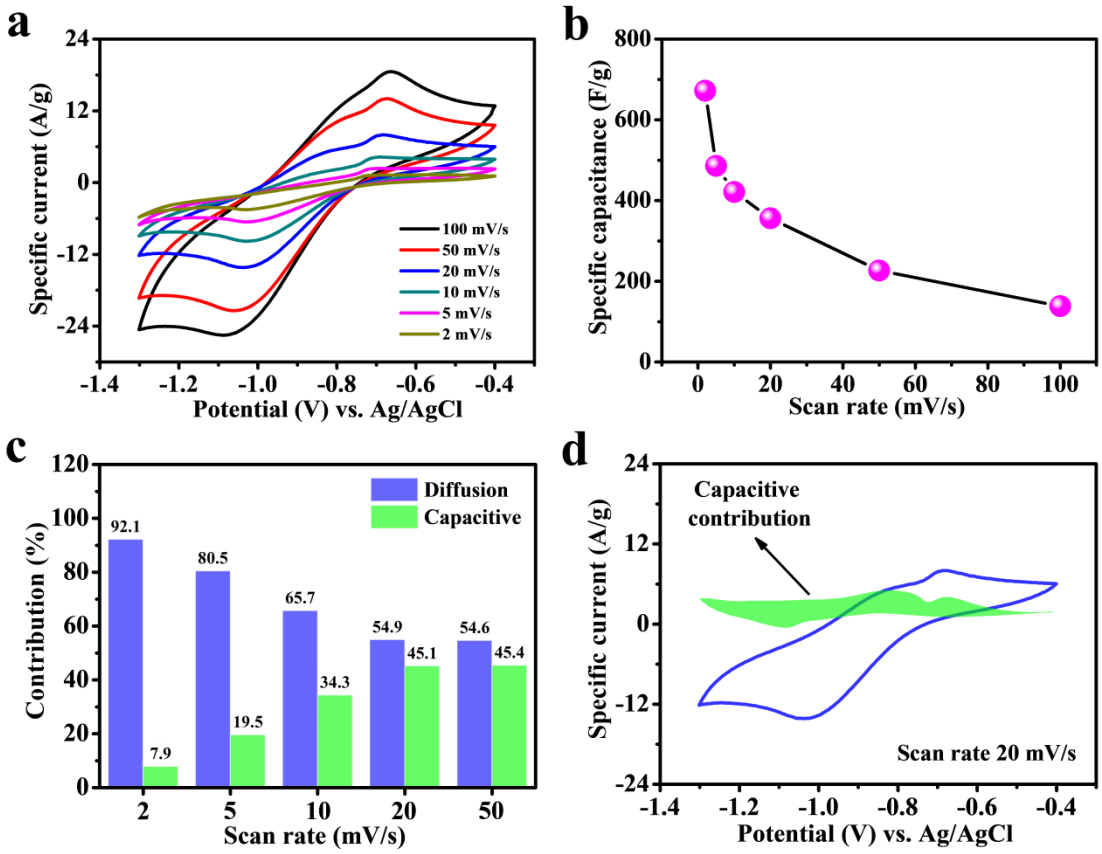

Figure 3 Electrochemical performances in 0.5 M NaOH electrolyte. (a) CV curves for iron selenide electrode with different scan rates. (b) Specific capacitance as function of scan rate. (c) Contribution ratio of the capacitive and diffusion-controlled charge of iron selenide electrode at various scan rates. (d) Separation of the capacitive and diffusion currents of electrode at a scan rate of 20 mV/s.

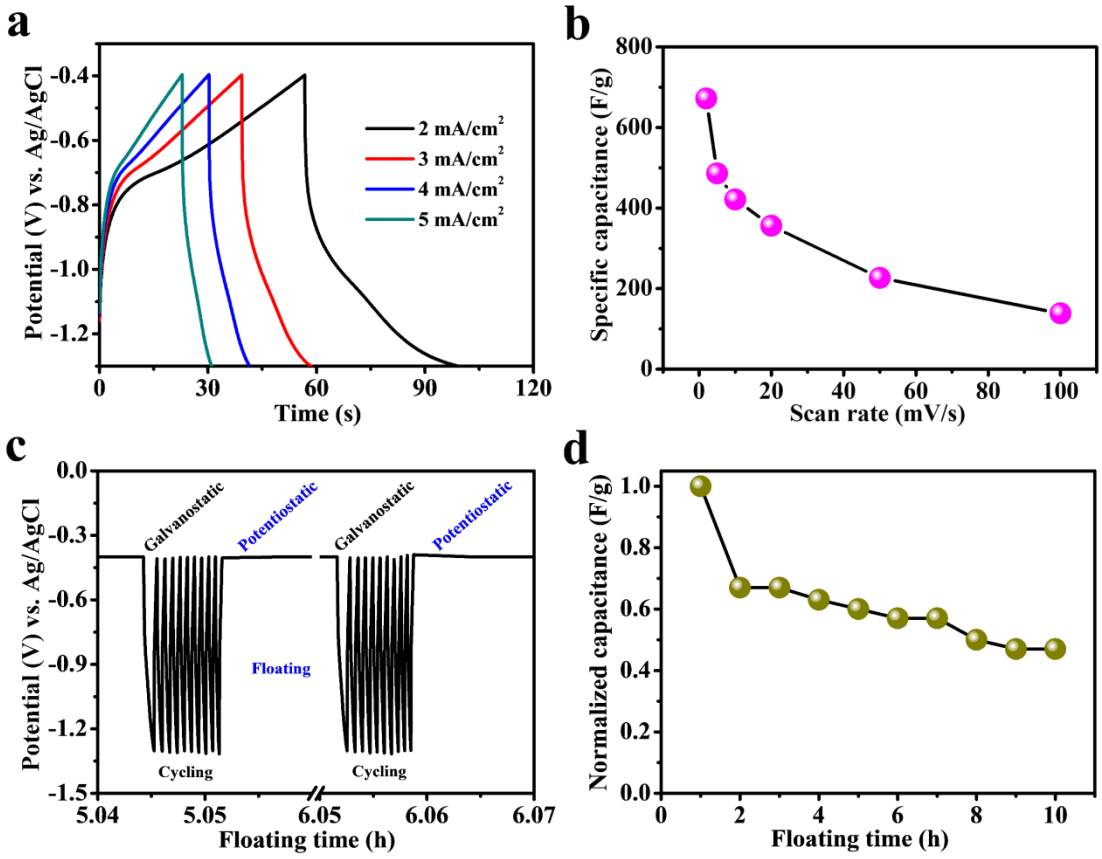

Figure 4 (a) GCD curves at different current densities ranging from 2 to 5 mA/cm^2. (b) Specific capacitance as function of current density. (c) Selected voltage profile during floating test experiment. (d) Normalized capacitance as a function of floating time.

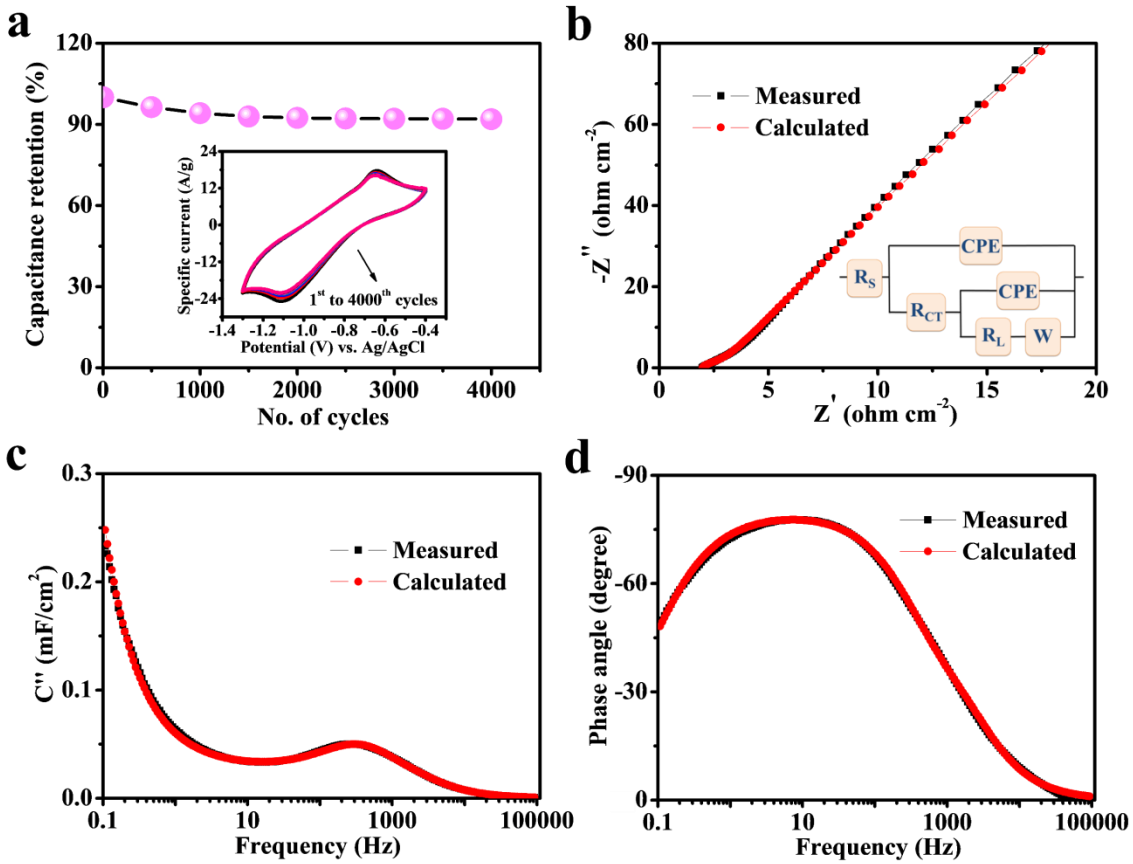

Figure 5 (a) Cycling stability of electrode for 4000 cycles at 100 mV/s scan rate, inset shows CV curves for various cycle numbers. (b) Nyquist plot of electrode in the range of 100 mHz to 100 kHz, inset shows matched equivalent circuit. (c) Imaginary capacitance vs. frequency plot. (d) Bode plot.

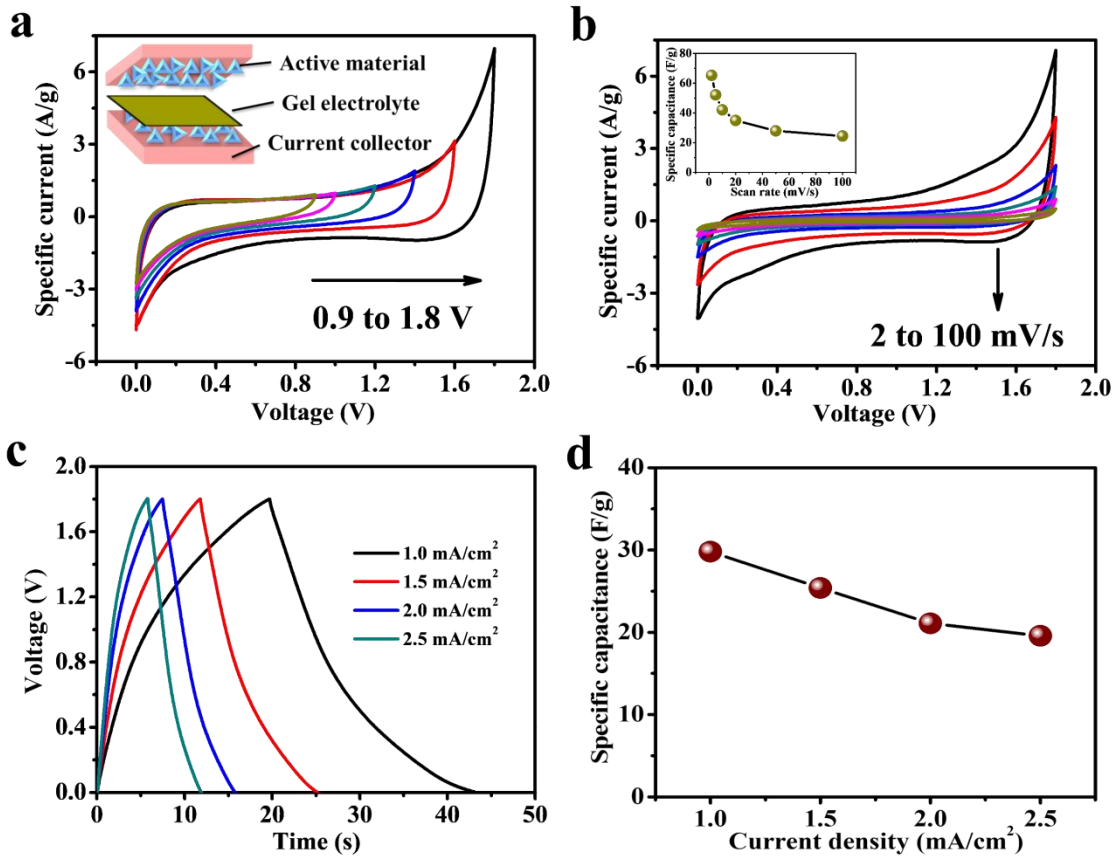

Figure 6 (a) CV curves of flexible solid-state cell collected at 100 mV/s scan rate in different voltage windows, inset shows schematic diagram illustrating the device configuration. (b) CV curves at various scan rates starting from 100 to 2 mV/s with voltage frame 1.8 V, inset shows specific capacitance at a function of scan rate. (c) GCD curves at various current densities ranging from 1 to 2.5 mA/cm^2. (d) specific capacitance as a function of current density.

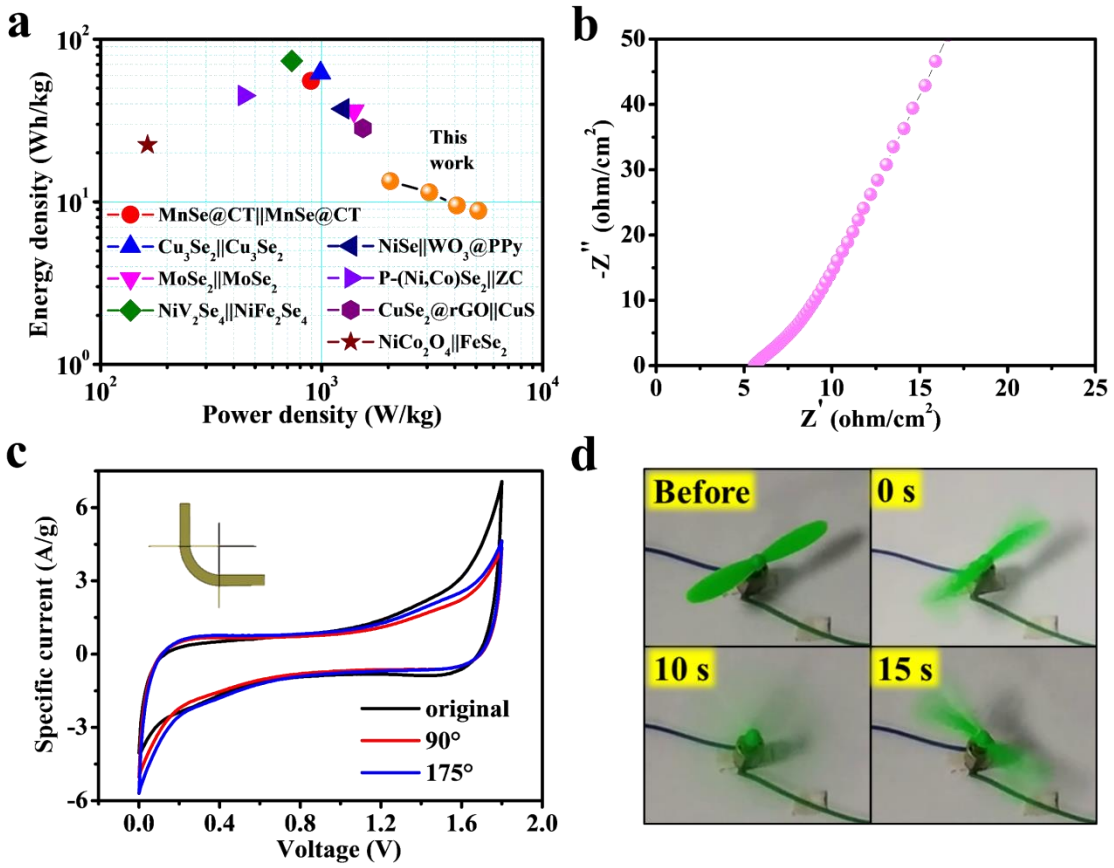

Figure 7 (a) Ragone plot, (b) Nyquist plot in frequency frame between 100 mHz to 100 kHz**.** **(**c) CV curves with specific bending angles at scan rate of 100 mV/s. (d) Motor fan powered by the manufactured cell for 15 s.

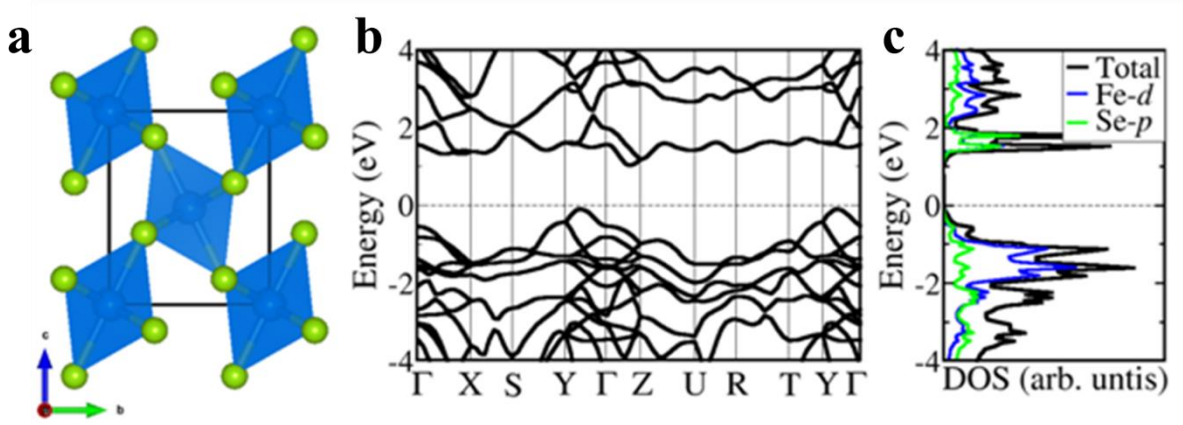

Figure 8 (a) The orthorhombic structure of iron selenide in terms of FeS_6 octahedra. (b) Band structure. (c) Partial density of states of iron selenide. (Atomic color: Fe = blue, Se = green).

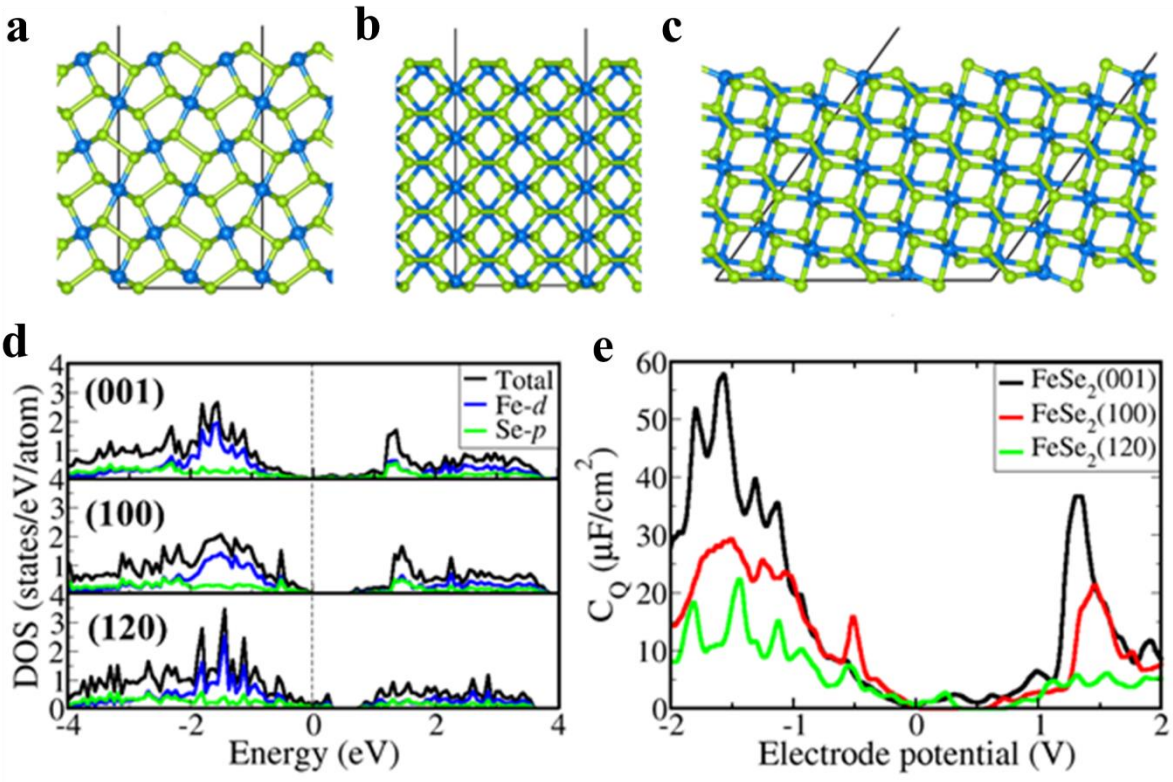

Figure 9 Geometry-optimized structures of (a) (001), (b) (100) and (c) (120) FeSe surfaces. The corresponding (d) partial density of states and (e) plot of Q_C with electrode potential for the different surface structures.

TOC (For Table of Contents Only)